Design and Analysis of a PM Synchronous Reluctance Generator for Light Vessels

Ileana Torac
Politehnica University Timisoara
Romanian Academy–Timisoara
Timisoara, Romania
ileana_torac@yahoo.com

Lucian Tutelea
Politehnica University Timișoara
Romanian Academy–Timisoara
Timisoara, Romania
lucian.tutelea@upt.ro

Spencer Goode-Kulchar
SPARK Lab, Pigman Eng. College
University of Kentucky
Lexington, KY, USA
spencer.goode-kulchar@uky.edu

Matin Vatani
SPARK Lab, Pigman Eng. College
University of Kentucky
Lexington, KY, USA
matin.vatani@uky.edu

Dan M. Ionel
SPARK Lab, Pigman Eng. College
University of Kentucky
Lexington, KY, USA
dan.ionel@ieee.org

Ion Boldea
Politehnica University Timisoara
Romanian Academy–Timisoara
Timisoara, Romania
ion.boldea@upt.ro

***Abstract*—This paper presents the design and analysis of a PM-assisted high-saliency synchronous reluctance machine (SynRM) intended for standalone operation in light vessels, according to industrial requirements. The machine is designed for 40–100 kW, 450–2400 rpm operation, with a regulated $800\ \mathrm{V}_{dc}$ output using a full-power active rectifier. The proposed machine features an axially laminated rotor with embedded permanent magnets on the q-axis, achieving high saliency ratios that enable reduced magnet usage and eliminate the need for overvoltage protection at high speeds. A preliminary analytical design methodology is employed to determine the geometry and operating characteristics, followed by comprehensive validation using the finite element method (FEM). The results demonstrate a peak torque of 932 Nm, high efficiency (up to 0.94), and favorable power factor across the operating range, along with reduced torque ripple through rotor segmentation. The machine maintains high performance under demanding operating conditions, including wide speed variation and constrained voltage operation. The proposed topology offers a practical, cost-effective solution with strong potential for industrial applications**

***Index Terms*—variable speed generator, hybrid electric vehicle, key FEM validation, axially-laminated rotor, variable speed drives, traction applications.**

I. Introduction

Standalone electric generators are widely employed in on-board vehicle applications [1–4], as well as in numerous stationary systems such as uninterruptible power supplies (UPS). A broad range of machine topologies have been investigated to meet the diverse requirements of these applications, particularly regarding efficiency, power density, controllability, and reliability.

Among the most prominent solutions are doubly fed induction generators (DFIG) [2, 5], which exhibit reduced efficiency and require power transfer through slip rings and brushes, leading to additional losses and maintenance requirements. Brushless DFIG (BDFIG) and reluctance generators [6] eliminate brushes but are generally limited by relatively low torque density and power factor. Three-stage d.c. excited synchronous generators (3-stage SG) [6, 7] provide brushless excitation, though they are characterized by slower dynamic response and increased machine volume.

Permanent magnet synchronous generators (PMSG) with surface-mounted magnets [8] offer high efficiency and compactness, yet their operation over a wide constant power speed range (CPSR) is constrained without additional protection at high speeds. Cage rotor induction generators (CRIG), including both single- and dual-stator configurations [4], are robust and cost-effective but suffer from relatively low torque density and reduced efficiency. Brushless double-saliency machines switched reluctance generators (SRGs or d.c. SRGs) [9] have been proposed, which are typically characterized with low torque density, poor power factor, and high electromagnetic force (EMF) harmonic content.

In addition to electromagnetic performance, the required power electronic interface plays a critical role in determining the overall system complexity and efficiency. The rating and type of power electronics needed to regulate the output depend strongly on both the generator topology and the desired output form (dc or ac). For dc output, DFIG, BDFIG, and CRIG with dual windings generally employ fractional-kVA PWM converters either in the rotor circuit or to supply the stator control winding, combined with a full-power diode rectifier at the output. In contrast, three-stage and dc excited synchronous generators require a low-power dc–dc converter PWM converter for field excitation, together with a full-power diode rectifier. Permanent magnet generators require either a diode rectifier followed by a full-power dc–dc converter converter or a full-power active rectifier to achieve the regulated dc output.

The selection of the most suitable generator topology depends on multiple factors, including application requirements and constraints on volume, weight, cost, safety, and manufacturing complexity. A common objective across all solutions is the achievement of an increasingly wide power–speed operating envelope while maintaining a constant, or

Table I
MAIN SPECIFICATIONS AND GEOMETRICAL PARAMETERS OF THE DESIGNED MACHINE.

Var.	Description	Value
P	Rated power [kW]	40–100
n	Speed range [rpm]	450–2400
$\eta_{\max}$	Efficiency at maximum speed [–]	0.94
T_{dens}	Maximum torque density [Nm/kg]	8
V_{dc}	DC voltage [V]	800
D_{so}	Outer stator diameter [mm]	306
D_{si}	Inner stator diameter [mm]	183.4
D_{sh}	Shaft diameter [mm]	82.0
g	Air-gap length [mm]	0.6
L_c	Core length [mm]	270.0
–	Stator and rotor lamination	Hyperco

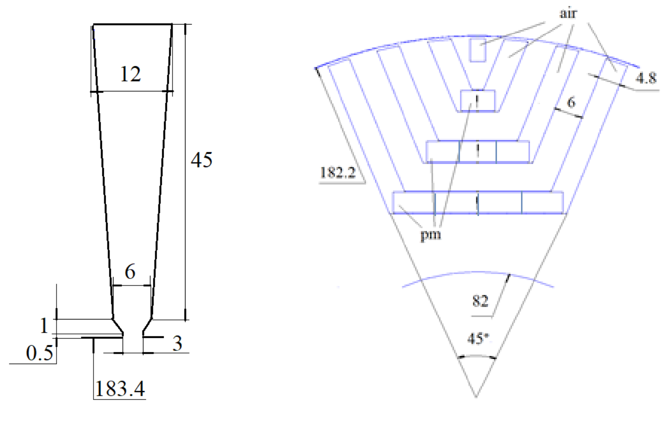

Figure 1. Main dimensions of the designed SynRM, illustrating (a) the stator slot geometry and (b) the rotor pole geometry.

minimally varying, regulated dc output voltage. In this context, PM-assisted rotor synchronous machine drives have been investigated for wide power–speed operation. The maximum saliency ratio achieved in such machines has typically been limited to L_d/L_q < 1.5–2.8 [10]. This implies a still significant contribution from the PMs, which in turn necessitates overvoltage protection at high speeds, particularly when the maximum rotor speed exceeds twice the base speed.

In this paper, a PM-assisted high-saliency ($L_d/L_q > 3.5$) reluctance synchronous generator is considered in conjunction with a full-power active rectifier for regulated dc operation output. This topology is selected based on its favorable characteristics. In particular, it offers high torque density (Nm/L and Nm/kg) and low copper losses (W/Nm). The use of a full-power active rectifier allows for effective control over a wide power–speed operating range, while maintaining relatively low rotor temperature, thereby simplifying thermal management and enhancing overall efficiency and power factor. The machine does not require overvoltage protection at maximum speed, as the induced emf remains below approximately 1.5 times the rated voltage. The proposed topology is compatible with established industrial manufacturing practices.

The main contributions of this paper are as follows. A PM-assisted synchronous reluctance generator with a high saliency ratio and reduced q-axis PM content is introduced to mitigate back-EMF at high speeds and avoid the need for overvoltage protection. A preliminary nonlinear analytical design methodology is developed for geometry sizing and performance prediction. The proposed design is subsequently validated through FEA, with results confirming the predicted performance in terms of power, voltage, d- and q-axis currents, efficiency, and power factor across the operating speed range.

II. DESIGN DATA

The analytical preliminary design is based on previous experience [11–16] and starts from the performance requirements and constraints concerning geometrical dimensions/limits. The main design ratings and geometric dimensions are listed in Table I. The key specifications, including rated power, operating speed range, voltage levels, and geometric constraints, are derived from industrial requirements for auxiliary generators in medium-sized yachts.

The stator design followed the approach in [11, 14, 15] with a double-layer winding, four parallel paths per phase, and 20 turns per coil. The stator slot dimensions are presented in Fig. 1(a). The rotor pole, shown in Fig. 1(b), has seven flux barriers per pole, with permanent magnets placed along the q-axis. The PMs are made of Neodymium Iron Boron (NdFeB) with a remanence of 1.18 T.

The width of the flux barriers is fixed at 4.8 mm for all barriers to simplify manufacturing and to allow the use of similarly sized magnets, enabling the purchase of standard PMs instead of custom-sized ones and resulting in a significant reduction in manufacturing costs. Additionally, to further simplify manufacturing and reduce cost and PM eddy current losses, the three PMs per pole are of a single size, with a different number of segments in each flux barrier (1, 3, and 4). Because q-axis space flux harmonics produce significant eddy currents in the rotor laminations, to reduce core losses and torque ripples, the solution is to build the rotor from segments, circumferentially shifted by an equivalent total skewing of one stator slot pitch.

III. KEY FEM ELECTROMAGNETIC VALIDATIONS

A. Peak Torque Operating Regime (T_{ek}=932 Nm at 435 rpm)

For the peak torque value of T_{ek} = 932 Nm, the corresponding current is obtained as i_{qk} = 141 A, assuming Ψ_{PM} = 0.5483 Wb under pure i_q control. The air-gap flux density distribution and the flux density distribution for the machine cross-section, corresponding to peak torque conditions with i_d = 65.72 A (peak), i_q = 141 A (peak), and a dq current angle of 24.99°, are presented in Fig. 2. Local high flux

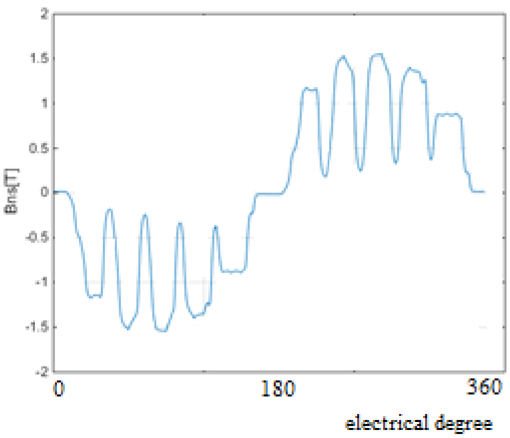

(a)

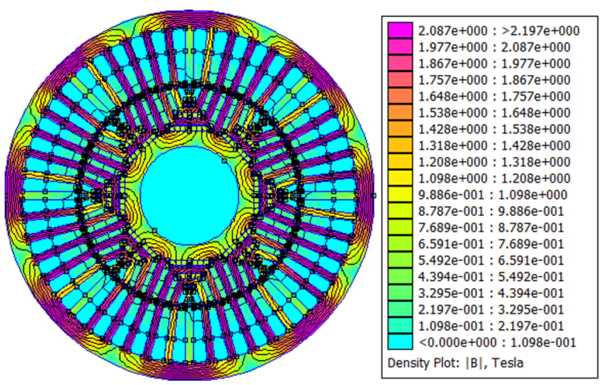

(b)

Figure 2. Air-gap flux density distribution (a) and flux density distribution across the machine cross-section under peak torque conditions (b).

density (Fig. 2(b)) is considered acceptable, as the machine volume was constrained from the outset of the design. The air-gap flux density at maximum torque, shown in Fig. 2(a), has a fundamental component that is in good agreement with the analytical design value, while also showing the strong fluctuations due to slotting effects due to the relatively small air-gap length.

Figure 5 portrays the d- and q-axis stator flux linkages; the relatively small ratio of $\Psi_{dk}/\Psi_{qk} \approx 0.2$ is indicative of a favorable power factor, targeted through a low current ratio of $i_{dk}/i_{qk} = 0.46$. The power factor can be approximated as:

$$\cos\varphi \approx \cos\left(\tan^{-1}\left(\frac{\Psi_{qk}}{\Psi_{dk}}\right) + \tan^{-1}\left(\frac{i_{dk}}{i_{qk}}\right)\right). \quad (1)$$

The resulting power factor at peak torque, as reported in Table II, is satisfactorily maintained at 0.7856. The torque is shown in Fig. 3 for both a straight rotor (T_e) and a three-segment rotor (T_m) with a total skew equivalent to one stator slot pitch. The anticipated peak torque of 932 Nm is validated by FEM, while the significant reduction in peak torque ripple due to rotor segmentation is clearly confirmed. The average torque remains practically unchanged, whereas

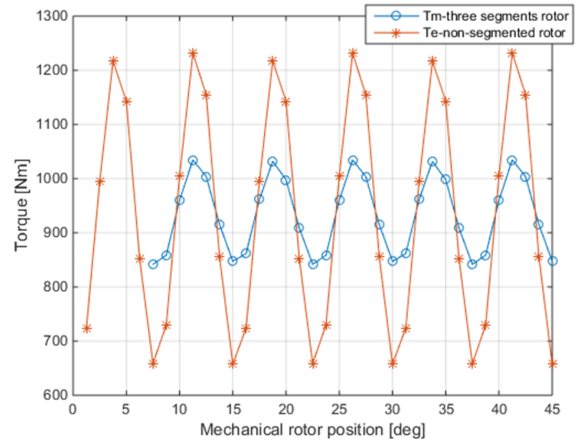

Figure 3. Machine torque for I_d = 65.72 A and I_q = 141 A (peak), with a d-q current angle of 24.99°, for a non-segmented rotor (T_e) and a three-segment rotor (T_m) with a total skew equivalent to one stator slot pitch.

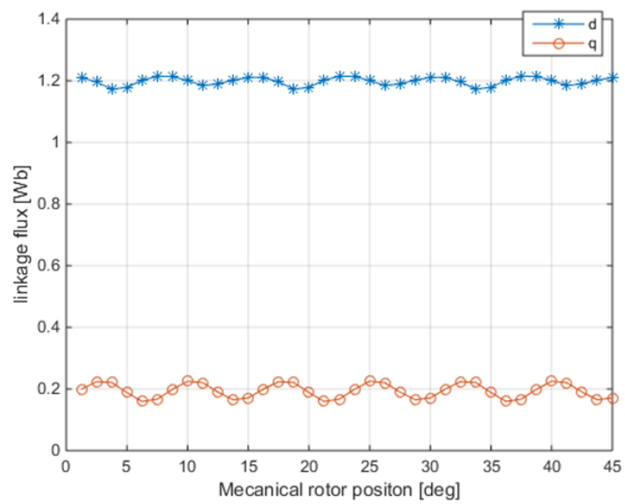

Figure 4. Stator d- and q-axis flux linkages of the machine for I_d = 65.72 A (peak) and I_q = 141 A (peak), with a d–q current angle of 24.99° (peak torque of 932 Nm).

in the segmented-rotor case, the torque ripple is reduced by a factor of 3.

To assess the risk of PM demagnetization, the magnetic flux density on the permanent magnet surfaces 1–6 is presented in Fig. 5. As observed, there is no risk of demagnetization under the peak torque operating regime. This is a crucial factor in ensuring a robust and reliable design.

The efficiency was evaluated by accounting for copper losses obtained from FEM, along with iron and mechanical losses as described in [16]. The stator core weight is 55 kg, the rotor core weight is 27 kg, the permanent magnets weigh 5 kg, and the stator winding weight is 28 kg. The main results for peak torque are synthesized in Table II.

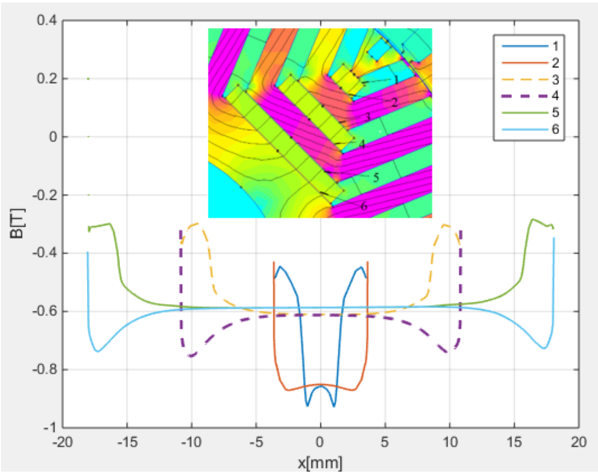

Figure 5. Magnetic flux density distribution on the PM surfaces.

Table II
MACHINE CHARACTERISTICS AT MAXIMUM TORQUE (932 NM, 450 RPM) AND MAXIMUM SPEED (317 NM, 2435 RPM).

Parameter	Symbol	Max Torque	Max Speed
Current	I_s [A]	110	80
Flux density	B_m [T]	1.24	0.56
Electromagnetic torque	T_e [Nm]	932.52	317.89
d-axis inductance	L_d [H]	0.0182	0.0248
q-axis inductance	L_q [H]	0.0053	0.0056
d-axis flux linkage	Ψ_d [Wb]	1.1981	0.4913
q-axis flux linkage	Ψ_q [Wb]	0.1942	0.0768
Power factor	$\cos\varphi$ [–]	0.7856	0.8317
Efficiency	η [–]	0.8726	0.948
Speed	n [rpm]	442	2435
d-axis current	I_d [A]	65.72	19.69
q-axis current	I_q [A]	141	111.39
Output power	P [kW]	43.16	81.06
Stator voltage (rms)	V_s [V]	224.72	507.23

B. Operation at n = 2435 rpm and T_e = 317.89 Nm

The air-gap flux density distribution and the flux density distribution on the machine cross-section, corresponding to peak speed currents of i_d = 19.69 A (peak) and i_q = 111.39 A (peak), are presented at the maximum speed of 2435 rpm in Fig. 6. As shown in Fig. 6(a), the combination of a relatively small i_d (19.69 A) and a still large i_q (111.39 A) at maximum speed results in greater variations of the air-gap flux density along the pole length, due to strong transverse armature reaction. As expected, the flux densities in the cores (Fig. 6(b)) are lower under these conditions compared to those at peak torque (Fig. 2). At n = 2435 rpm, with i_d = 19.69 A (peak) and i_q = 111.39 A (peak), the stator voltage is V_s = 507.16 V, which is below the maximum allowable value of 509 V (at V_{dc} = 800 V). The efficiency is η = 0.948, and the power factor is $\cos\phi$ = 0.8317, as reported in Table II.

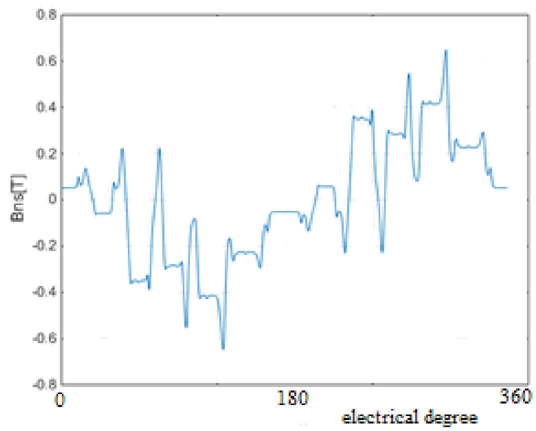

(a)

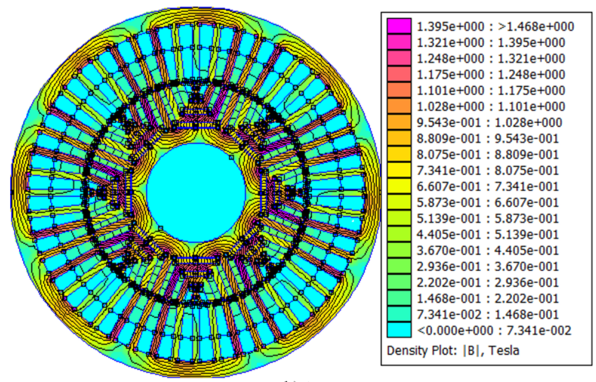

b)

(b)

Figure 6. Air-gap flux density distribution (a) and flux density distribution across the machine cross-section (b) for I_d = 19.69 A and I_q = 111.39 A (peak), with a d–q current angle of 10.02°.

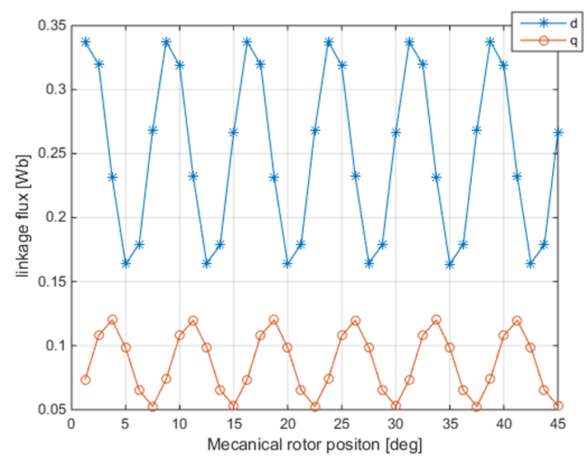

Figure 7. The machine d and q-axis linkage flux for I_d=19.69 A(peak), I_q = 111.39A(peak), d-q current angle 10.02°.

The d-q flux linkage for I_s = 80 A (RMS), corresponding to i_d = 19.69 A and i_q = 111.39 A (peak), with a d-q current angle of 23.75° as a function of mechanical rotor position,

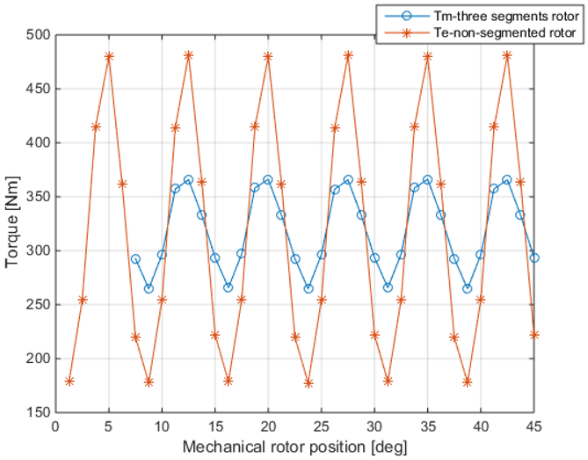

Figure 8. Machine torque for I_d = 19.69 A (peak) and I_q = 111.39 A (peak), with a dq current angle of 10.02°, for a non-segmented rotor (T_e) and a three-segment rotor (T_m) with a total skew equivalent to one slot pitch.

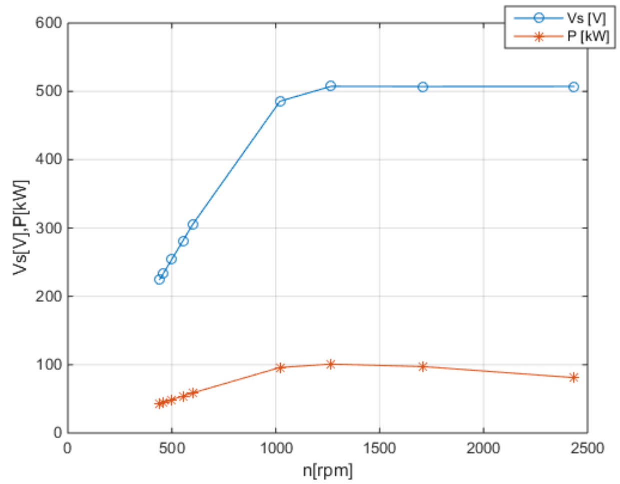

Figure 10. The power and voltage versus speed.

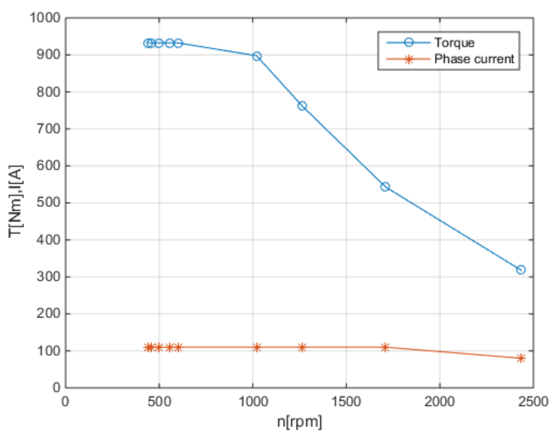

Figure 9. The torque and the phase current versus speed.

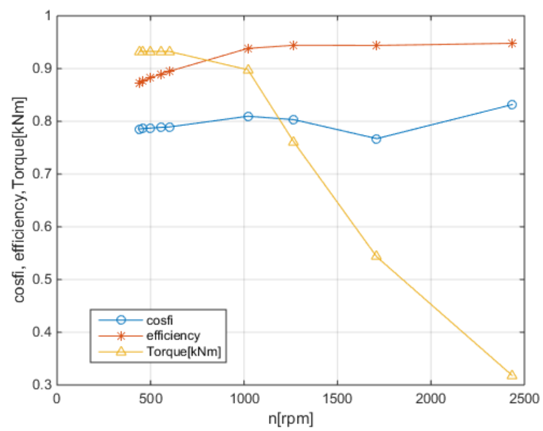

Figure 11. The torque, efficiency, and power factor versus speed.

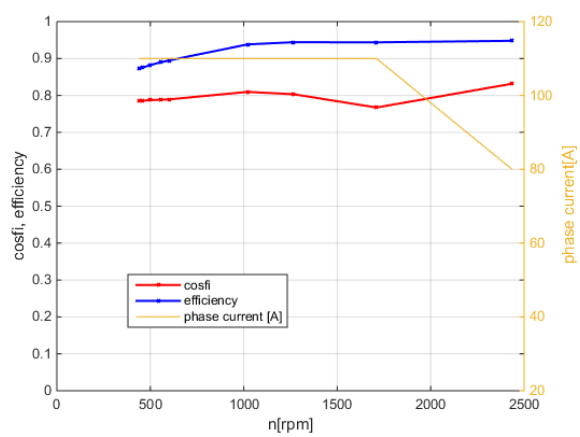

Figure 12. The efficiency, power factor, and phase current factor versus speed.

is shown in Fig. 7. The machine torque for both a straight rotor (T_e) and a three-segment rotor (T_m) with a total skew equivalent to one stator slot pitch, is presented in Fig. 8. The average torque remains practically unchanged, while in the segmented rotor case, the torque ripple is reduced by approximately a factor of 3.

FEM simulations for numerous other operating points were considered to assess the machine's ability to meet the design requirements. The torque-speed variation is shown in Fig. 9. It highlights a fairly constant torque between 420 and 1020 rpm, followed by a linear decrease in torque (from 898 Nm to 318 Nm) at higher speeds (up to 2435 rpm).

To obtain these results with limited current, as illustrated in Fig. 9, the phase voltage below 1000 rpm was allowed to be significantly lower than the maximum value of V_{1s} = 505 V (RMS) per phase, as shown in Fig. 10. This implies that the active rectifier must provide sufficient voltage boost to maintain a constant DC output of 800 V_{dc} over the entire speed range of 450–2435 rpm, or alternatively, that a dc-dc converter must be incorporated for this design with its particularly challenging power–speed operating range, as depicted in Fig. 11. However, at speeds above 1000 rpm, the machine delivers relatively constant output power and voltage, as shown in Fig. 10, with an efficiency of 0.93–0.94.

The efficiency and power factor as functions of speed are presented together with the torque (in kNm) in Fig. 11 and with the phase current in Fig. 12, providing a comprehensive view of the machine behavior across all FEM-investigated operating points. As shown in Fig. 10, the output power P reaches 100 kW at 1266 rpm, corresponding to i_d = 40.26 A (peak), i_q = 150.26 A (peak), and a d–q current angle of $15°$.

IV. Conclusion

The paper proposed a solution for a PM-assisted reluctance synchronous generator with high saliency (L_d/L_q = 3.43 at maximum torque and 4.42 at maximum speed), rated at approximately 40–100 kW over a speed range of 450–2400 rpm, delivering an 800 Vdc output without requiring overvoltage protection at high speeds. For Tek = 932 Nm and a machine active specific torque of 8.1 Nm/kg, the design achieves a high torque-to-magnet ratio of 932 Nm/5 kg, corresponding to 186 Nm/kg of PM. However, the wide speed range (450–2435 rpm) and the requirement to deliver at least 50 kW at the lowest speed (450 rpm), while maintaining relatively high efficiency (0.8726) and power factor (0.7856) at peak torque (932 Nm), necessitate operation with a reduced output voltage. Consequently, the active rectifier must provide sufficient voltage boost to maintain a constant 800 V_{dc} output across the entire speed range.

The key FEM validation results confirm that the proposed solution delivers strong performance at moderate cost, using standard manufacturing processes, across all investigated torque–speed operating points. Nevertheless, for a more comprehensive assessment of the design, further detailed studies—including advanced FEM analysis, thermal and mechanical evaluations, optimization, prototyping, and experimental validation—are required in future work.

References

[1] D. Kumar and F. Zare, "A comprehensive review of maritime microgrids: System architectures, energy efficiency, power quality, and regulations," *IEEE Access*, vol. 7, pp. 67 249–67 277, 2019.

[2] Y. Lin, Y. Liu, W. Xu, M. G. Hussien, and E. M. Rashad, "An improved speed observer based on super-twisting algorithm for standalone brushless doubly-fed induction generator-dc system," in *International Conference on Electrical Machines and Systems (Online)*. IEEE, 2022, pp. 1–6.

[3] S. Kato, N. Hoshi, and K. Oguchi, "A low-cost system of variable-speed cascaded induction generators for small-scale hydroelectricity," in *Conference Record of the 2001 IEEE Industry Applications Conference. 36th IAS Annual Meeting (Cat. No.01CH37248)*, vol. 2. IEEE, 2001, pp. 1419–1424 vol.2.

[4] K. Rajashekara, "Power electronics for more electric aircraft," in *Power Electronics for Renewable Energy Systems, Transportation and Industrial Applications*. IEEE Press/Wiley, 2014, ch. 12, pp. 365–386.

[5] P. Mondal, M. Malakar, P. Tripathy, S. Krishnaswamy, and U. Saha, "Robust observer design for sensorless voltage and frequency control of a doubly fed induction generator in standalone mode," *IEEE transactions on energy conversion*, vol. 37, no. 2, pp. 844–854, 2022.

[6] Y. Liu, W. Xu, T. Long, and F. Blaabjerg, "An improved rotor speed observer for standalone brushless doubly-fed induction generator under unbalanced and nonlinear loads," *IEEE transactions on power electronics*, vol. 35, no. 1, pp. 775–788, 2020.

[7] C. Mi, M. Filippa, J. Shen, and N. Natarajan, "Modeling and control of a variable-speed constant-frequency synchronous generator with brushless exciter," in *Conference record of the 2003 IEEE Industry Applications Conference : 38th IAS Annual Meeting : IAS 2003 : October 12-16, 2003, Salt Lake City*, vol. 1. IEEE, 2003, pp. 562–567 vol.1.

[8] N. K. Finaviya, V. R. R. Rudraraju, and K. Venkatraman, "A mppt control scheme for standalone pmsg system with single active bridge," in *2017 International Conference on Intelligent Computing, Instrumentation and Control Technologies (ICICICT)*. IEEE, 2017, pp. 457–462.

[9] L. Yu, Z. Zhang, Z. Chen, and Y. Yan, "Analysis and verification of the doubly salient brushless dc generator for automobile auxiliary power unit application," *IEEE transactions on industrial electronics (1982)*, vol. 61, no. 12, pp. 6655–6663, 2014.

[10] R. D. Naik, J. Kavil Kambrath, and P. Agarwal, "Investigation of stability issue of ipm starter/generator for more electric aircraft," in *2023 IEEE International Conference on Power Electronics, Smart Grid, and Renewable Energy (PESGRE)*, 2023, pp. 1–7.

[11] L. Tutelea, A. M. Popa, and I. Boldea, "50/100 kw, 1350-7000 rpm (600 nm peak torque, 40 kg) pm assisted reluctance synchronous machine: Optimal design with fem validation and vector control," in *2014 International Conference on Optimization of Electrical and Electronic Equipment (OPTIM)*. IEEE, 2014, pp. 276–283.

[12] M. Aydin and M. K. Guven, "Comparing various pm synchronous generators: A feasible solution for high-power, off-highway, series hybrid, electric traction applications," New York, pp. 36–45, 2014.

[13] Y. Lu, J. Li, H. Xu, K. Yang, F. Xiong, R. Qu, and J. Sun, "Comparative study on vibration behaviors of permanent magnet assisted synchronous reluctance machines with different rotor topologies," *IEEE transactions on industry applications*, vol. 57, no. 2, pp. 1420–1428, 2021.

[14] I. Boldea, *Reluctance Synchronous Machines and Drives*. Oxford University Press, 05 1996. [Online]. Available: https://doi.org/10.1093/oso/9780198593911.001.0001

[15] I. Boldea and L. Tutelea, *Reluctance electric machines: design and control*. CRC press, 2018.

[16] R. Richter, *Kurzes Lehrbuch der elektrischen Maschinen: Wirkungsweise, Berechnung, Messung*. Berlin: Springer, 1949.